Materials & Design 268 (2026) 116450

Contents lists available at ScienceDirect

Materials & Design

journal homepage: www.elsevier.com/locate/matdes

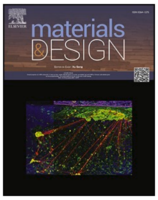

Machine learning–assisted grain boundary segmentation reveals nanoscale heat treatment behavior of additively manufactured 316L stainless steel

Shiro Ihara [a,*], Shunsuke Sato [b], Ryosuke Ozasa [c,d], Takayoshi Nakano [c,d], Mitsuhiro Murayama [a,e]

[a] Institute for Materials Chemistry and Engineering, Kyushu University, Kasuga 816-8580, Japan
[b] Interdisciplinary Graduate School of Engineering Sciences, Kyushu University, Kasuga 816-8580, Japan
[c] Division of Materials and Manufacturing Science, Graduate School of Engineering, The University of Osaka, 2-1 Yamadaoka, Suita, Osaka 565-0871, Japan
[d] 3DPTec Integrated Center, Graduate School of Engineering, The University of Osaka, 2-1 Yamadaoka, Suita, Osaka 565-0871, Japan
[e] Department of Materials Science and Engineering, Virginia Tech, Blacksburg, VA 24061, USA

ARTICLE INFO

Keywords:
Electron microscopy
Machine learning
Laser powder bed fusion
Heat treatment
Grain boundary

ABSTRACT

Additive manufacturing produces inhomogeneous and anisotropic microstructures that differ from those in conventionally processed materials. Heat treatment is a crucial process to regulate the microstructural properties. Although estimating the resultant microstructure is a challenging issue, visualizing grain boundaries (GBs) would provide fundamental understanding of the mechanism during heat treatment. In this study, we developed a visualization method using electron diffraction mapping in transmission electron microscopy combined with machine learning. By extracting the area where the feature of electron diffraction patterns varies in the mapping data, GB region was successfully visualized. The developed image processing was applied to ex-situ heating observation of an additively manufactured 316L stainless steel (316L SS), and the curvature variation of GB before and after heat treatment was discussed. It was shown that GB bulging was likely observed around existing sub-GBs, causing unevenness in GB migration.

1. Introduction

Additive manufacturing (AM) enables unprecedented control over component geometry, yet it produces complex microstructures due to rapid solidification [1–3]. The resultant microstructure is in non-equilibrium state characterized by, for instance, pronounced dislocation cell structure and segregation of solute atoms [4]. These inhomogeneity in the microstructure lead to anisotropy of mechanical properties and residual stress [5–7], those of which are often undesirable for industrial purposes. After heat treatment, the microstructure becomes more homogeneous and stable compared to that in the as-built condition. Elucidating the microstructure evolution before and after heat treatment is essential for controlling and optimizing mechanical properties, and many studies have addressed this issue (e.g., [8–11]). However, the detailed mechanisms of microstructure evolution during heat treatment are still not fully understood due to unique microstructural factors, such as the high density of localized dislocations and segregated solute atoms [8,12,13]. The high dislocation density increases the driving force, while the solute atoms inhibit the grain boundary (GB) migration. In any cases, visualizing details of GB morphology in nanoscale helps investigating the fundamental mechanisms and kinetics of GB migration, as well as how the microstructural factors influence the resultant morphology.

On the other hand, the visualization of GB in nanoscale is not a trivial issue. Electron backscatter diffraction (EBSD) technique using scanning electron microscopy (SEM) typically becomes the common method for visualizing GB morphology [12,14,15]. However, only the traces of GBs appear on the sample surface can be detected in SEM because the detectable electrons are limited to the vicinity of surface, thus the detail of GB migration would be difficult to obtain. X-ray diffraction microscopy is a powerful technique for visualizing GBs in 3D [16,17]. However, the spatial resolution is typically around 1 μm, which is not sufficient for elucidating the influence of dislocation structures and nanosized precipitates in detail. A suitable nanoscale visualization technique would be the dark field (DF) imaging using transmission electron microscopy (TEM), where a selected diffraction spot is used for imaging 18,19. DF imaging can reveal whole grain shape when the most suitable diffraction spot is selected. 3D visualization of crystal grains at

---

* Corresponding author.
E-mail address: ihara-shiro@cm.kyushu-u.ac.jp (S. Ihara).

https://doi.org/10.1016/j.matdes.2026.116450
Received 13 April 2026; Received in revised form 16 June 2026; Accepted 17 June 2026

nanoscale has been achieved [20], namely, all the GBs in the observed field of view can be visualized by this method. However, the challenges of DF-based visualization lie in the selection of an appropriate diffraction spot, as described below. First, it is not obvious which diffraction spot visualizes a whole single grain. When certain diffraction spots originating from two adjacent crystal grains are identical, these spots must be avoided for visualizing their GBs. Second, there are multiple factors, such as local strains that can fluctuate or smear the diffraction spot intensity from a crystal grain [21,22]. Diffraction spot(s) free from those factors should be selected for clear GB imaging. Third, which is related to the first and the second, recording DF images while avoiding these problems is labor-intensive and sometimes not feasible, especially when the region of interest contains a large number of GBs or dislocations. A convenient, as well as robust visualization technique should be established to analyze a broad range of materials.

In this study, we developed a GB visualization method by combining electron diffraction mapping and machine learning-assisted image processing. The electron diffraction mapping, also known as 4D-STEM (four-dimensional scanning transmission electron microscopy) [23,24], has been attracting attention because of its capabilities for nanoscale analysis. This method records a 2D electron diffraction pattern from each point of the region of interest, rather than a specific spot. Thus, the obtained data consists of a set of 2D electron diffraction patterns holding the 2D real space coordinates of the region of interest. While electron probe scanning from one crystal grain to the adjacent grains, electron diffraction patterns from the first grain gradually alters to those of the adjacent ones around GBs [19]. In principle, the gradual variation can be measured by expressing each electron diffraction pattern as a linear combination of the representative electron diffraction patterns, which will be obtained by averaging the electron diffraction patterns of each grain recorded in the grain interior. Then, the variation is to be characterized by a clustering method. The points where the variation ends will be obtained by fitting the coefficient variation in each clustered area using Gaussian process regression and by detecting the crossing points. The detected points should be regarded as the edge of GBs.

This paper demonstrates the development of GB detection from electron diffraction mapping data. We first employed a conventional austenitic steel sample to develop and validate the image processing procedure. Then, the developed method is applied to ex-situ heating observation of an additively manufactured 316L SS. Comparison of the GB morphology before and after heat treatment clearly reveals the inhomogeneous GB migration near sub-GBs.

2. Methods

2.1. Data acquisition

ASTAR (NanoMEGAS) [25] system installed to an ARM200F (JEOL) electron microscope operated at an acceleration voltage of 200 kV was used for electron diffraction map acquisition. ASTAR enables to yield precise electron diffraction patterns by the precession of electron beam [26,27].

The sample for image processing procedure development was an Fe-22Mn-0.6C steel (FCC). The bulk sample was thinned to electron transparency by mechanical polishing followed by Ar^+ ion milling using model IB-09060CIS cryo ion slicer (JEOL). Electron diffraction mapping was performed with a precession angle of 0.5° and 10 nm step size. The second condenser lens aperture size was 10 μm, camera length was 300 mm and the image size of the diffraction pattern was 288 × 288 pixels. After the electron diffraction mapping, crystal orientation of each grain was determined through template matching [28] using the software bundled with ASTAR. Although the orientation map indicates lines distinguishing crystal grains, they express only a part of GB regions because GBs are two-dimensional crystal defects, appearing as surface in general. These lines tentatively express GBs and are noted as ‘initial-GB’ hereafter. The data on the initial-GB was also to be processed in the same way as that in grain interior.

A TEM foil from additively manufactured 316L SS sample was prepared as follows. The feedstock powder was obtained from EOS GmbH (Germany). The LPBF process was carried out using an EOS M290 system (EOS, Germany), with the laser power P, scanning speed v, scanning pitch D, and stacking thickness t set to $P = 250$ W, $v = 800$ mm/s, $D = 0.08$ mm, and $t = 0.06$ mm, respectively. Bulk samples with dimensions of 10 mm × 10 mm × 10 mm were fabricated in an Ar atmosphere by employing bi-directional laser scanning in one direction for all layers. The bulk sample was sliced along a [100] direction, and then thinned down by mechanical polishing followed by Ar^+ ion milling. Electron diffraction mapping was performed with a precession angle of 1.0° and 10 nm step size. Then, the TEM foil was heat treated at 1000℃ for 10 min under Ar atmosphere using a tubular electric furnace (Asahi Rika Manufacturing Co., Ltd.), and cooled by Ar flow. The identical field of view was examined using the same acquisition parameters for direct comparison. It should be noted that the objective of this experiment was to capture the early stage of recrystallization. Based on some literatures [9,29], which indicated recrystallization in additively manufactured 316L SS occurred at around 1000°C given sufficient time, the heat treatment condition used in this study (1000°C for 10 min) was determined accordingly.

2.2. Image processing procedure

2.2.1. Feature extraction from electron diffraction mapping data

The detection strategy of GB is to identify regions where electron diffraction patterns vary around the initial pattern. In this concept, diffraction patterns in identified GB region overlap with those from other crystals. Fig. 1 shows the overall flow of the GB detection. The aim up to the multivariate least squares (MLS) fitting step (labeled A in Fig. 1) is to quantitatively express how much electron diffraction patterns vary within two adjacent grains. In the step, first, mask images corresponding to each grain were created using the orientation map as shown in Fig. 2(a). These mask images tentatively defined which regions an electron diffraction pattern belongs to. Second, electron diffraction patterns were averaged within a mask to obtain representative electron

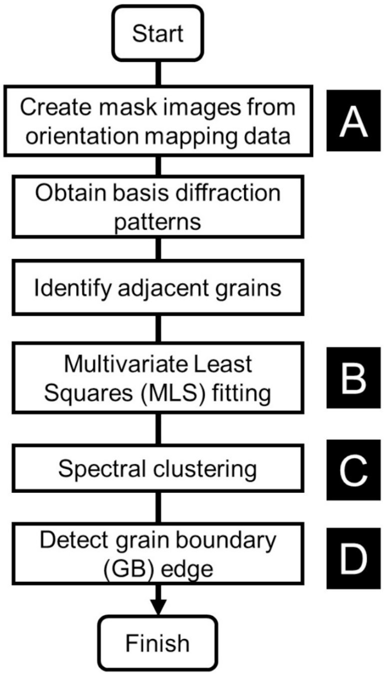

Fig. 1. Flowchart of GB extraction. Details of processes A to D are indicated in later figures.

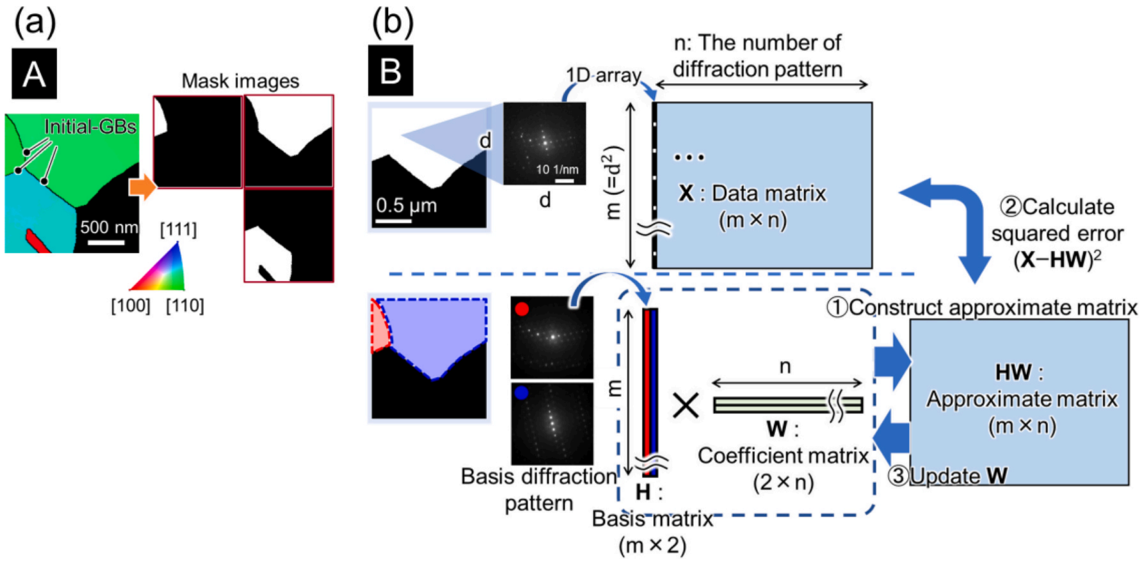

Fig. 2. Schematic illustration showing image processing procedure A and B, which are indicated in Fig. 1, respectively. (a) Image processing procedure of A. Mask images were created based on an orientation map, which was obtained via template matching of electron diffraction mapping data. (b) Image processing procedure of B, showing summary of MLS fitting. MLS fitting was performed for each two adjacent grains. Electron diffraction patterns at each point were flattened to 1D array, making the data matrix (**X**). The basis diffraction patterns were obtained by averaging electron diffraction patterns within a crystal grain, which had been identified in (a). The basis matrix (**H**) was created by flattening the basis diffraction patterns and concatenating them. The coefficient matrix (**W**) was initially defined in random value. Then, **W** was repeatedly updated so that minimizing the error between the approximate value (**HW**) and **X**.

diffraction patterns. Hereafter, the created electron diffraction patterns in this way are called 'basis diffraction patterns'. These basis diffraction patterns enabled to express each electron diffraction pattern as a linear combination of those as demonstrated in a later section.

After identifying which grains were neighbors, MLS fitting, a type of multivariate statistical analysis [30], was applied (labeled B in Fig. 1) using NumPy library (version 2.2.6) [31]. Summary of this fitting procedure is shown in Fig. 2(b). To quantitatively represent the variations among electron diffraction patterns, an electron diffraction pattern ($\boldsymbol{X}$) at point p is approximated by using the basis diffraction patterns ($\boldsymbol{H}$):

$$\boldsymbol{X}_p \approx \sum_i w_{i,p} \boldsymbol{H}_i, \tag{1}$$

where i indicates the number of targeted grains and the coefficient $w_{i,p}$ means contribution from basis i at point p ($p = 1\ n$). $w_{i,p}$ is the variable to be obtained. In this step, MLS fitting was implemented for each pair of grains ($i = 1, 2$) to ensure the mathematical independency in the basis diffraction patterns. If three or more basis diffraction patterns are defined, one of the basis diffraction patterns may be expressed as a linear combination of others, and consequently, the uniqueness of the solution is no longer guaranteed. In Fig. 2(b), the coefficient matrix $\boldsymbol{W}$, composed of $w_{i,p}$, was initially defined with arbitrary values, and the matrix $\boldsymbol{HW}$, which approximates $\boldsymbol{X}$, was constructed. Then, the squared error of these two matrices ($(\boldsymbol{X} - \boldsymbol{HW})^2$) was calculated and $\boldsymbol{W}$ was updated to minimize the error.

Fig. 3(a) indicates the representative $w_{1,p}$ and $w_{2,p}$ distribution after the MLS fitting. $w_{1,p}$ and $w_{2,p}$ were predominant in both left-hand side (Grain1) and right-hand side (Grain2) grains, respectively. The predominant coefficient clearly varied around the expected GB. A line profile obtained along the broken line in Fig. 3(a) quantitatively demonstrates the variation of coefficients. In Fig. 3(b), two breakpoints (BPs) were clearly appeared. Fig. 3(c) shows the corresponding electron diffraction patterns around the BPs. At the BP1, the signal intensity of electron diffraction from Grain2, e.g., marked by blue circles, started to be intense while that from Grain1, e.g., marked by red circles, started to be diminished. Behind the BP2, the signal intensity of the electron diffraction from Grain1 disappeared and that from Grain2 became dominant. Therefore, the BPs can be regarded as the edge of GBs.

2.2.2. GB detection

As shown in Fig. 3(b), the GB region was expressed as the slope in $w_{i,p}$ distribution profile. In other words, the variation of $w_{i,p}$ in the GB region was roughly linear, while that within the crystal grain was roughly negligible. Based on the concept, we performed spectral clustering [32] (labeled C in Fig. 1), by defining the similarity matrix as follows:

$$A_{pq} = \exp\left(-\|w_{i,p} - w_{i,q}\|/2\sigma^2\right), \tag{2}$$

where A_{pq} is (p, q) component of the similarity matrix ($q = 1\ n$), $\|\bullet\|$ means L2 norm, σ is the constant which indicates how sensitively signal changes are detected. In this study, we used the coefficient of the basis of Grain2 ($i = 2$), $\sigma = 0.2$ in the case of the austenitic steel, $\sigma = 0.1$ in the case of the 316L SS. The tuning of σ was necessary depending on the input data. Wrong choice of σ resulted in undesired outputs, as shown in Fig. S1. In the case of 316L SS, changes in diffraction signal intensity occurred frequently within the grains because they contained a high density of dislocations. To clearly distinguish the signal variations between the grain interiors and the GBs, a smaller σ value was needed. The spectral clustering means that images such as Fig. 3(a) is regarded as a graph structure, where each edge weight between node p and node q are given by A_{pq}. The weight is predominantly determined how much the coefficient at point p matches that at point q. Since the coefficient within the crystal grains is almost same, the difference of that around a point ($\|w_{i,p} - w_{i,q}\|$) is nearly zero. At GBs, on the other hand, $\|w_{i,p} - w_{i,q}\|$ around a point is larger than that inside the crystal grains. The graph defined in this way can characterize the coefficient variation. The spectral clustering partitions the graph such that similar structure is assigned to the same group by applying k-means clustering to the eigenvectors of the graph Laplacian. In this study, the MLS result for each pair of crystal grains was classified into three with the aim of dividing the targeted dataset into Grain1, Grain2, and GB, respectively. Only a fixed width of region from initial-GB as shown in Fig. 4(a) was considered for computational efficiency and balance the number of data points. The calculation width in Fig. 4(a) was 30 pixels (300 nm) in the case of the austenitic steel and 50 pixels (500 nm) in the case of for the 316L SS in this study.

Fig. 4(b) shows the representative result of the clustering. Intuitively,

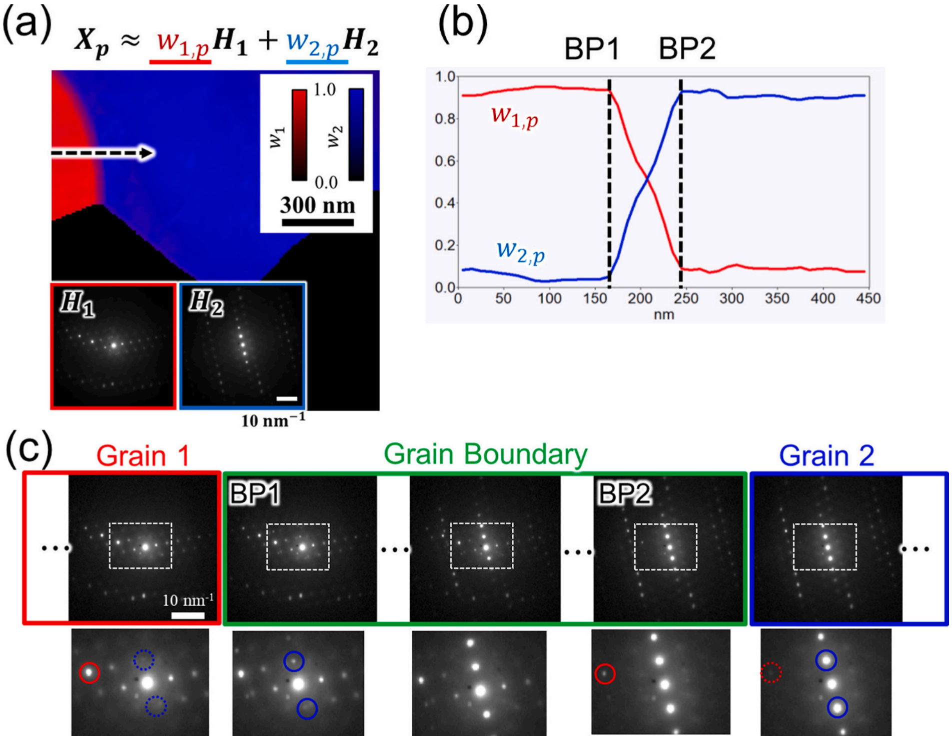

Fig. 3. A representative result of MLS fitting. (a) Distribution of coefficients for the basis $\mathbf{H}_1$ and $\mathbf{H}_2$. The dotted arrow indicates where the line profile (b) taken from. From (b), GB would be assumed to be between the breakpoint 1 (BP1) and BP2. (c) Electron diffraction patterns corresponding to the line profile. Their magnified view was also shown. Looking from left to right, the diffraction spots marked by the blue circles started to appear at BP1, and the intensity of them gradually increased. The intensity of the diffraction spot marked by the red circle, on the other, gradually decreased from BP1. Then, the diffraction spot disappeared after BP2. Therefore, the region between BP1 and BP2 corresponded to GB. (For interpretation of the references to colour in this figure legend, the reader is referred to the web version of this article.)

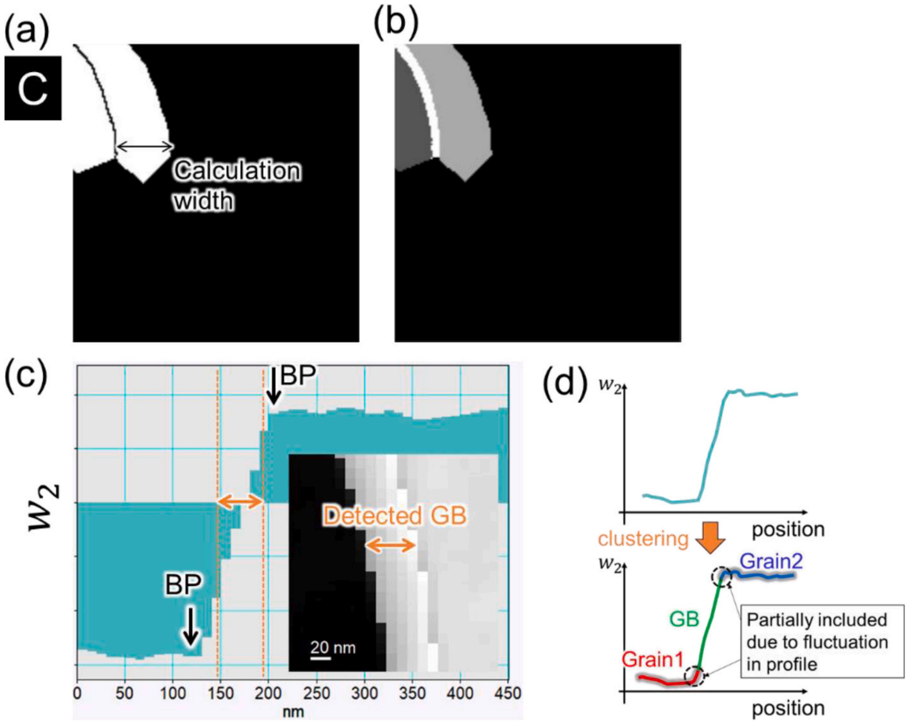

Fig. 4. Summary of spectral clustering, which is labeled C in Fig. 1. (a) Definition of input data region. Only the data within a distance from the initial-GB (calculation width) was used in the clustering. (b) Representative results of spectral clustering. (c) Quantitative evaluation of the clustering results. By comparing the clustering results with a line profile of a MLS result, the detected GB was found to be underestimated. (d) Schematic drawing how spectral clustering underestimated the GB width.

the result appears to be divided into Grain1, Grain2, and GB, respectively. However, superposition of the $w_{2,p}$ distribution and the clustering result indicated that the GB region obtained by the clustering was always located between the BPs as shown in Fig. 4(c). This result indicates that the clustering must have underestimated the width of the GB. The underestimation would be an inevitable consequence in this clustering. As noted, $w_{2,p}$ (also $w_{1,p}$) gradually varied from Grain1 to Grain2, while it showed roughly constant inside the crystal grains, although there was some fluctuation. The fluctuation in the profile within the crystal grains somewhat yields coefficient variation, which is considerably smaller than that at GB center. However, the coefficient variation around the BPs is also not large compared to that at the GB center. Therefore, the BPs and their surrounding points would likely be regarded as identical to the crystal grains rather than as GBs, as schematically indicated in Fig. 4 (d).

To summarize here, the spectral clustering enabled to roughly identify the three regions – Grain1, Grain2, and GB. The identified GB region was underestimated, and thus, the BPs, namely GB edge, were to be detected (labeled D in Fig. 1) using the clustered data as demonstrated in next section. Although the clustering did not exactly yield GB region, we tentatively note the clustered region as Grain1, Grain2, and GB for convenience in the following section.

2.2.3. GB edge detection

Fig. 5(a) shows the flowchart of the GB edge detection step labeled D in Fig. 1. This proposed approach aimed to detect intersections of three curvilinear surfaces derived by Gaussian process regression [33] using the coefficient distribution inside each clustered region, Grain1, Grain2, and GB, obtained from the previous clustering step. Fig. 5(b) schematically indicates the basic concept of the GB edge detection. This concept is built upon the MLS outcomes in which the coefficient variation is roughly monotonic for each region as shown in Fig. 3(b). Three regression functions expressing the coefficient distribution within the interior of individual clustered regions can be defined, and these should be monotonic over the entire regions of interest. The intersections of these three regression functions indicate both ends of a GB, that is, two BPs as indicated in Fig. 5(b). In here, these regression functions were obtained through Gaussian process regression, using the coefficient distributions in each clustered region as inputs. This process is labeled (ii) in Fig. 5(a). The resultant functions were represented as three curvilinear surfaces that express the coefficient distributions of each region, and the extrapolations of these curvilinear surfaces intersected near the 'GB' assigned in the previous step. Then, the region between the two intersections was designated as 'tentative GB', label-(iii) in Fig. 5(a). If there was no significant deviation between the curvilinear surface (regression function) over the GB and the original coefficient distribution data (the corresponding MLS result) exists within the tentative GB region, the GB edge detection step is completed.

It should be noted that using all clustered regions without separation as the input for the regression step is not feasible, because all the clustered regions are adjacent and intersections coincide with the cluster boundaries, making GB edge detection impractical. The resultant regression functions, or curvilinear surfaces, from such input would be similar to those shown by the orange dotted lines in Fig. 4(c), and thus this step offers no improvement. To resolve this, GBs edge (BP) were assumed to be located within a certain distance from a GB. Each identified crystal grain was then subsequently shrunk to generate a gap, d, as indicated in Fig. 5(c) (label- (i) in Fig. 5(a)). The gap was configured to be 3 ($d = 3$[pixels]) and was later confirmed to be not sensitive to the accuracy of the GB detection because the input region has adaptively changed as described in later paragraph.

For the regression surface construction, we used $w_{2,p}$ distribution within each region and performed the Gaussian process regression using Matern kernel [34] expressed as follows,

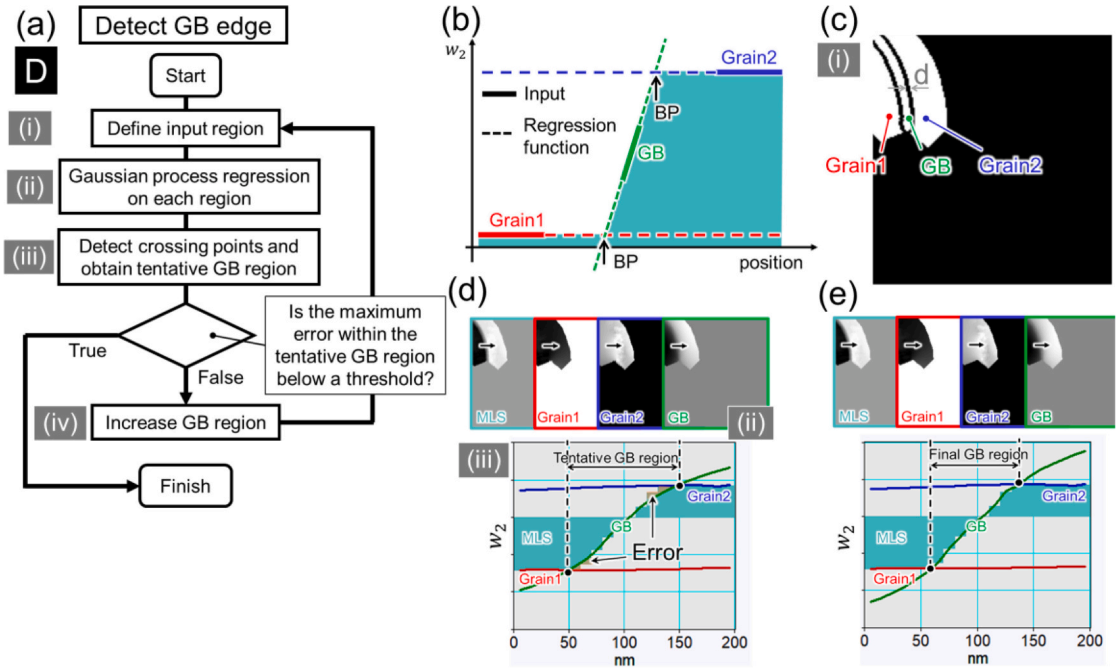

Fig. 5. Summary of GB edge detection, which is labeled D in Fig. 1. (a) Flowchart of the process. (b) Schematic drawing of the GB edge detection method procedure. (c) Definition of the data input region for Gaussian process regression. Using the results of the spectral clustering, the three kinds of region were defined (Grain1, Grain2, and GB). Each crystal grain was shrunk by the distance d. The GB edge was assumed to lie between the GB and shrunk regions. The Gaussian process regression was performed using the coefficient distribution in each region as input. (d) Results of gaussian process regression at first loop. Since the GB edge was estimated by extrapolating the regression curve, the error between the MLS result (original data, light blue) and the regression curve was sometimes inevitable. One pixel was added at the GB positions closest to the points showing error above threshold (more than 5% in this study). This process corresponded to "increase GB region" in (a). (e) Results of gaussian process regression after finishing the loop, showing the adequately fitted regression curves. (For interpretation of the references to colour in this figure legend, the reader is referred to the web version of this article.)

$$k(w_{2,p}, w_{2,q}) = \frac{1}{\Gamma(\nu)2^{\nu-1}}\left(\frac{\sqrt{2\nu}}{l}d_e(w_{2,p}, w_{2,q})\right)^{\nu} K_{\nu}\left(\frac{\sqrt{2\nu}}{l}d_e(w_{2,p}, w_{2,q})\right), \tag{3}$$

where $d_e(\bullet)$ means the Euclidian distance, $K_\nu(\bullet)$ means a modified Bessel function, and $\Gamma(\bullet)$ means the gamma function. The Gaussian process regression estimates a surface without assuming a specific functional form, yielding a surface that fits well for any input data while retaining its smoothness in the extrapolation region. In this study, ν was set to 0.5 to make the curvilinear surfaces as flat as possible and to ensure only a single intersection per line profile. The gaussian process regression was carried out using the scikit-learn library [35].

Fig. 5(d) indicates the obtained curvilinear surfaces using the data in Grain1 (marked by red), Grain2 (blue), and GB (green), with the original MLS result as a reference (light blue). The figure also shows the line profiles at the position indicated by an arrow, representing the intersections between Grain1 and GB and Grain2 and GB, respectively. The intersections roughly corresponded with the BPs. However, some errors between the line profile of the regression surface and the original MLS data were detected within the GB region as shown in Fig. 5(d). The errors indicate that the variation of regression surface was gentler than the MLS data, resulting in the overestimation of the GB width. When the maximum error within the tentative GB exceeded the threshold value, which was 5% in this study, an update, i.e., the change of the GB width, labeled (iv) in Fig. 5(a), was carried out by dilating by 1 pixel at the edge of the GB region closest to the position where error exceeded the threshold. Then, the gap d from the updated GB region was set and all the input regions were redefined for the Gaussian process regression. These processes were iteratively performed until all the errors in tentative GB region were less than 5%. Note that the error threshold was set to be below average error after the first loop of each pair of grains. The average error value for each pair was shown in Fig.S2.

Fig. 5(e) demonstrates the same data plot as Fig. 5(d) but obtained at the final step of the GB edge detection. In the figure, the intersections showed good agreement with the BPs. Therefore, the obtained intersections corresponded with the GB edges. By filling inside of the detected GB edges, whole GB region was obtained.

3. Results and discussion

To summarize the image processing, the variation of electron diffraction patterns in the electron diffraction mapping data was first expressed as the feature variation – the variation of coefficients which were obtained through MLS fitting. The region where the coefficients vary was regarded as a GB, and was detected using the spectral clustering and the Gaussian process regression. In this section, we evaluated the accuracy of the GB detection and then applied to ex-situ heating observation of an additively manufactured 316L SS in which GB migration occurred.

3.1. *Evaluation of the proposed method*

To alternatively reveal GB region from the electron diffraction mapping data, we performed virtual dark field (VDF) imaging [36]. In VDF, an image is reconstructed from the signal of specific areas in electron diffraction patterns, instead of physically using a DF aperture during imaging. By selecting the diffraction spots appropriately, the VDF image showing a single crystal grain can be obtained as shown in Fig. 6 (a). This VDF image was reconstructed from the three diffraction spots indicated in the same figure. The multiple selection of the diffraction spots enabled to visualize the crystal grain with enough contrast, and therefore, by choosing appropriate threshold value, the mask image that corresponds the single crystal grain was obtained. Hereafter, mask images obtained from VDF images are called VDF mask.

We obtained VDF masks for the three crystal grains and superimposed them to create a combined mask. Fig. 6(b) left shows the combined VDF mask, where the GB region clearly appeared. The middle of Fig. 6(b) indicates the GB region obtained from the proposed method. This GB region was obtained by combining the extracted GB regions for each pair of the crystal grains. The overlapped image of the two is shown in Fig. 6(b) right, where the common region was demonstrated as white. In the figure, 97% of the points matched. The average distance among the mismatched points, excluding the points that were outside the three crystal grains, was 1.1 pixel (11 nm). We applied same procedure to several tilt angles (±20°) as shown in Fig. S4. The results were also in agreement with the VDF images to a similar extent as described above, despite the increase in effective foil thickness caused by sample tilting.

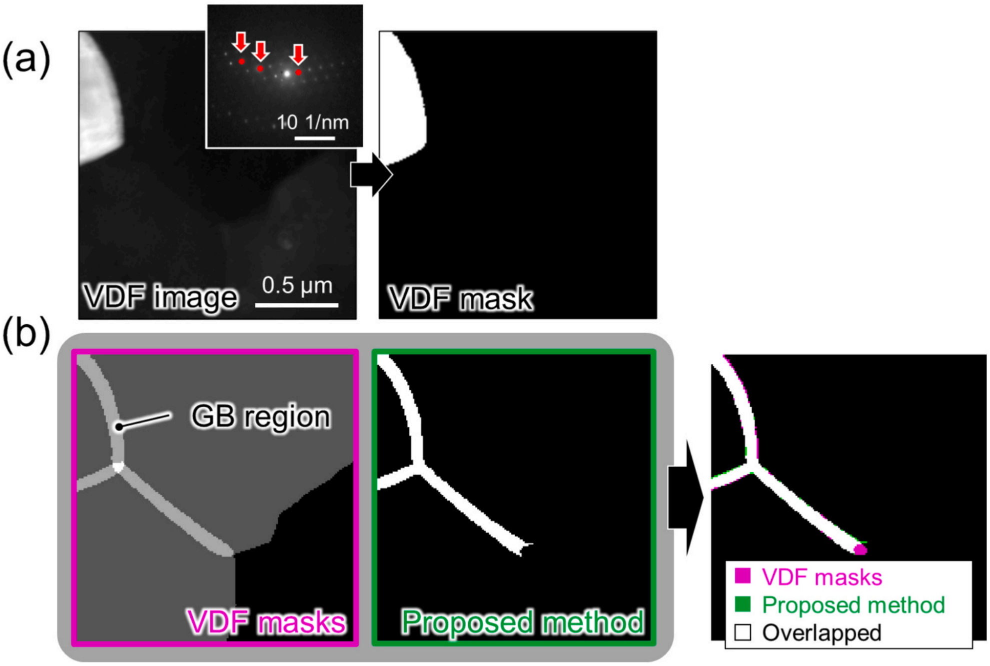

Fig. 6. Validation of GB detection. (a)Procedure of VDF mask creation. (b) Comparison of combined VDF masks with proposed method.

Therefore, the proposed method successfully extracted the GB area from the electron diffraction mapping data. Note that a gap formed around the triple junction of the GB after simply combining the extracted GB regions. The gap was only a few pixels and surrounded by the extracted GB regions, and thus, it was filled by interpolation.

It should also be noted that the GB extraction using VDF demands suitable diffraction spots selection and threshold value determination, thus careful handling is needed. When diffraction spots that also appear also in neighboring crystal grains are selected, both crystal grains will be highlighted and cannot be distinguished. The suitable threshold value depends on which and how many diffraction spots are selected since the selected area determines the signal intensity of a VDF image. In this study, the threshold value was determined from the signal intensity of neighbor regions near GB edge for each VDF image because the intensity of electron diffraction spots is likely influenced by structural defects and sample thickness. The proposed method in this study does not require the diffraction spot selection and the threshold determination, and thus, provides more objective and more noise-robust approach.

3.2. *Application to ex-situ heating observation*

Fig. 7(a) shows virtual bright field (VBF) images of the additively manufactured 316L SS sample presenting an identical GB region before and after heating. The VBF images were reconstructed from the signal intensity of transmitted wave in electron diffraction patterns, and thus they are equivalent to regular STEM-BF images. Many dislocations were observed in the sample before heating, whereas the number of visible dislocations decreased after heating when observed from same orientation. Fig. 7(b) presents the corresponding orientation maps, where crystal grains with the misorientation angle larger than 10° are indicated. Only the band-shaped contrast in the central region in Fig. 7(a) was the high angle GB, thus all other band-shaped contrast areas were concluded to be sub-GBs. Fig. 7(c) shows the GB area extracted using the proposed method. Overall morphological changes induced by heating were clearly observed; however, determining the exact distances remains challenging at present because of the lack of invariant point. Adding fiducial markers or applying image correlation methods will be the subject of future study. Note that to obtain Fig. 7(c), we vertically divided the MLS results into five, i.e., five stripes of coefficient distribution were prepared as input for the clustering step. This division was needed because electron diffraction patterns differed slightly even within a single crystal grain due to the sub-GBs included in this field of view. Dividing the input data can reduce its variability, making clustering more effective.

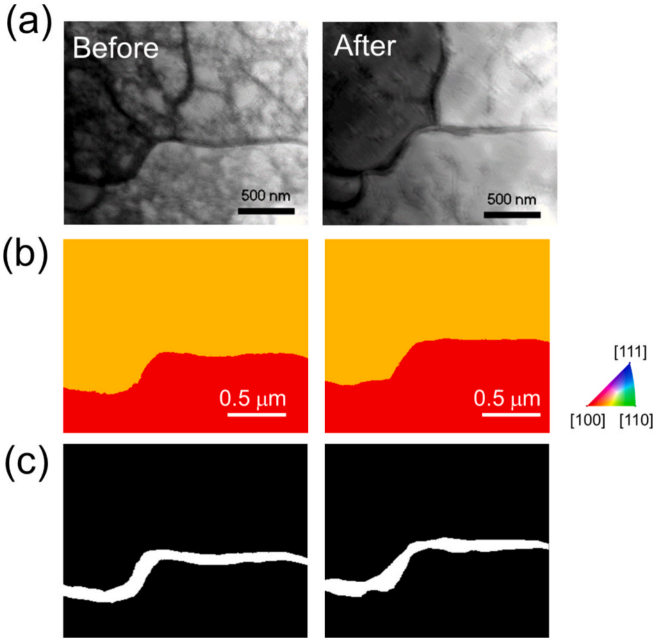

Fig. 7. Summary of ex-situ heating observation for an additively manufactured 316L SS. (a) VBF images before and after heating. (b) Orientation maps showing crystal grains with high misorientation angle (more than 10 deg.). (c) Results of GB detection using the proposed method based on (b).

To quantitatively compare the variation, we evaluated the absolute curvature of the detected GB edges. The curvature calculation was performed after fitting the GB edges as Chebyshev polynomial such that the fitting parameter minimizing the Akaike's information criterion. This fitting procedure prevents overfitting while minimizing error, resulting in smooth fitting, and enables theoretical calculation of the derivatives. We have confirmed by using mathematical models that the fitting results matched with theoretical solution of the curvature distribution and robust in noise addition as shown in Fig.S3. Fig. 8(a) shows the curvature distribution of the entire field of view. To examine the curvature variation in detail, three areas were selected as indicted by I to III in the figure. Fig. 8(b) compares the shapes of these three GB edges before and after heating, side by side, where the average curvature in the region of interest is also shown. The curvature of the GB edge basically decreased as representatively shown in Fig. 8(b) left. The decrease of curvature after heating was easily understood because heating process generally reduces the free energy of materials. However, one of the areas showed increase of the curvature after heating as expressed in Fig. 8(b) right.

To examine what caused the GB edge geometry variation, we compared the VBF images of each area with their corresponding extracted GBs as shown in Fig. 9(a). The area where curvature increased (III) was merged with a sub-GB, resulting in the concave shape after heating as indicated in the green arrow. Another area where another sub-GB merged (II) also showed the concave shape. These results would indicate that GB bulging was likely observed around sub-GBs during heating in this study, sometimes yielding high curvature GBs. This sub-GB induced GB migration has also been proposed [12]. According to the literature, crystal grains containing sub-GBs have higher elastic strain energy than neighboring crystal grains, resulting in the promotion of grain nucleation at sub-GB junction based on the strain induced boundary migration (SIBM) mechanism [37–39] and leading to the convex shape of GBs. Multiple studies have reported the SIBM in many materials [40–42] and the results shown in Fig. 9(a) supports the SIBM in the 316L SS. Interestingly, in the after-heating sample of Fig. 9(a), the width of the GBs around the sub-GB junction was small compared to the surrounding GB region. If the sub-GBs contributed the GB bulging isotropically, the GB width would be constant. The concave morphology in the GB region suggests that GB bulging straightens the inclined GBs, leading to a reduction in the GB interfacial area and thus the interfacial energy.

It should be noted that another area also showing concave shape as indicated by orange arrow in Fig. 9(a) would form by the presence of precipitates. Fig. 9(b) shows an electron diffraction pattern around the sub-GB. Diffraction spots not belonging to the matrix (austenitic steel, FCC) appeared. A VDF image reconstructed using one of those spots (Fig. 9(c)) indicates fine precipitates aggregated around the GB. These precipitates slightly decreased the signal intensity of the diffraction spots from the matrix. When the signal intensity of diffraction spots from the matrix decreased, the coefficient ($w_{i,p}$) in Eq. (1) would become smaller compared to the crystal grain interior. Consequently, the precipitates located at the GB were also classified as part of the GB region. This classification is a natural consequence of the proposed method, which identifies GB regions based on the overlap of diffraction patterns with those from adjacent crystals. While understanding the nature of grain boundary precipitation is a critical topic in materials science, and the development of evaluation methods for grain boundary microstructures is certainly valuable, these topics are beyond the scope of the present work and will be addressed in future studies.

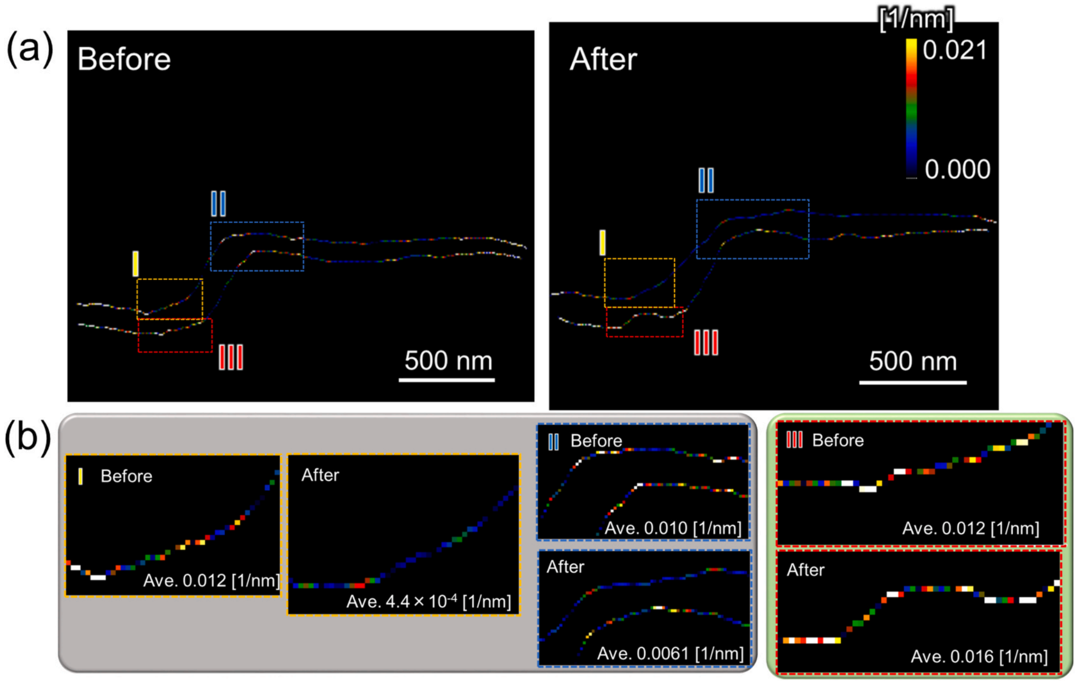

Fig. 8. Quantitative evaluation of detected GB edges. (a) Curvature distribution for whole field of view. (b) Magnified field of view whose number and region were indicated in (a).

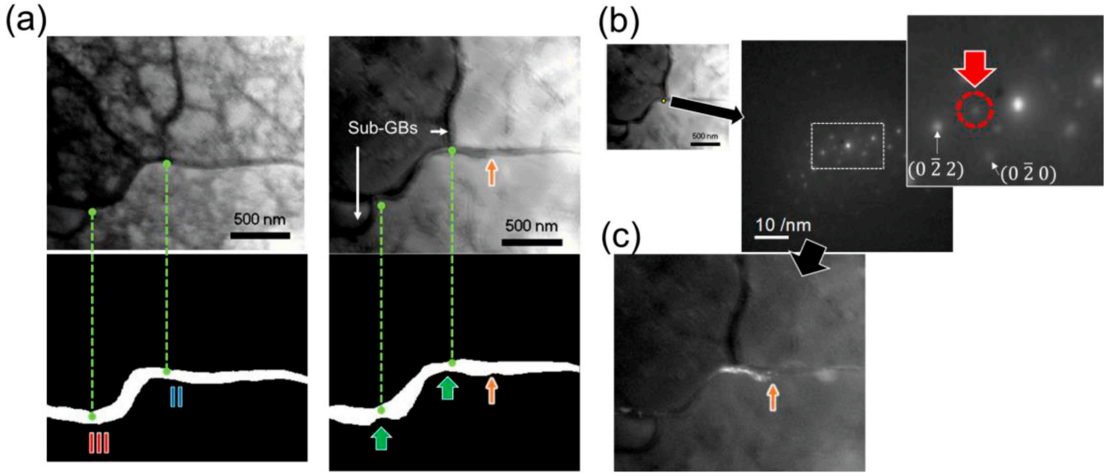

Fig. 9. Details of morphological changes induced by heating. (a) Redisplay of VBF images and extracted GBs. The green dotted lines indicate the parts of GB connected with sub-GBs. The displayed numbers correspond to those in Fig. 8(a). (b) An electron diffraction pattern extracted at the GB, showing diffraction spots which were not belong to the matrix. (c) A VDF image created by using the spot shown in the dotted red circle in (b). The convex shape indicted by orange arrows in (a) and (c) likely formed by precipitates. (For interpretation of the references to colour in this figure legend, the reader is referred to the web version of this article.)

4. Conclusion

This paper demonstrated the machine learning-assisted image processing for GB extraction from electron diffraction mapping data. Calculating the feature variation in electron diffraction patterns and detecting the points where the feature variation completed made it possible to visualize the GB region. The proposed method was validated to be comparable to the other visualization method, VDF. The advantage of the proposed method lies in the objective determination of the GB region, and thus, it enables to quantitatively analyze the GB edge shape.

The visualization method was also applied to ex-situ heating observation of an additively manufactured 316L SS. The curvature variation before and after heat treatment was discussed. It was demonstrated that GB bulging was likely occurred around sub-GBs during heating. As demonstrated in this study, the proposed method would reveal the variation of GB morphology under external stimuli in detail for broad range of materials.

5. Funding sources

This study was supported by JSPS KAKENHI Grant Numbers JP24K17494, JP25H00805, JP23H00238. R.O. and T.N. were supported in part by JSPS KAKENHI Grant Numbers 23H00235 and 25K00051 and CREST-Nanomechanics: Elucidation of Macroscale Mechanical Properties based on Understanding Nanoscale Dynamics for Innovative Mechanical Materials (grant number JPMJCR2194) from the Japan Science and Technology Agency (JST).

CRediT authorship contribution statement

Shiro Ihara: Writing – review & editing, Writing – original draft, Visualization, Validation, Supervision, Software, Project administration, Methodology, Investigation, Funding acquisition, Formal analysis, Data curation, Conceptualization. **Shunsuke Sato:** Software, Methodology, Investigation, Formal analysis, Data curation, Validation, Visualization, Writing – original draft. **Ryosuke Ozasa:** Writing – review & editing, Writing – original draft, Validation, Resources, Investigation, Funding acquisition. **Takayoshi Nakano:** Writing – review & editing, Resources, Investigation, Funding acquisition. **Mitsuhiro Murayama:** Writing – review & editing, Writing – original draft, Validation, Supervision, Resources, Methodology, Funding acquisition.

Declaration of competing interest

The authors declare that they have no known competing financial interests or personal relationships that could have appeared to influence the work reported in this paper.

Acknowledgments

The authors acknowledge Dr. Punyafu and Satoko Kaku for their assistance with TEM sample preparation.

Appendix A. Supplementary data

Supplementary data to this article can be found online at https://doi.org/10.1016/j.matdes.2026.116450. Supplementary information: sensitivity of the parameter in spectral clustering (Fig.S1); error between MLS results and regression curves after first loop (Fig.S2); validation of Chebyshev polynomial fitting using Akaike's information criterion (Fig. S3); grain boundary segmentation from dif- ferent tilt angle data (Fig. S4).

Data availability

The code used in this study is available at https://github.com/shiro-ihara/gb_extraction. The diffraction mapping data will be made available on request.

References

[1] A. Hemmasian Ettefagh, S. Guo, J. Raush, Corrosion performance of additively manufactured stainless steel parts: a review, Addit. Manuf. 37 (2021), https://doi.org/10.1016/j.addma.2020.101689.

[2] Z. Hu, Y. She, L. Hua, K. Dong, M. Chen, Y. Wang, X. Qin, Non-planar additive manufacturing: a comprehensive review of path planning, system integration, process control, and applications, Addit. Manuf. 115 (2026) 105059, https://doi.org/10.1016/j.addma.2025.105059.

[3] H. Chen, D. Egusa, Z. Li, T. Sasaki, R. Ozasa, T. Ishimoto, M. Okugawa, Y. Koizumi, T. Nakano, E. Abe, Phase-separation induced dislocation-network cellular structures in Ti-Zr-Nb-Mo-Ta high-entropy alloy processed by laser powder bed fusion, Addit. Manuf. 102 (2025), https://doi.org/10.1016/j.addma.2025.104737.

[4] K. Cho, K. Yamashita, S. Kakutani, T. Saito, T. Sasaki, K. Sawaizumi, M. Okugawa, Y. Koizumi, T. Mayama, T. Kikukawa, O. Gokcekaya, T. Ishimoto, H. Kimizuka, W. Gong, T. Kawasaki, S. Harjo, T. Nakano, H.Y. Yasuda, Effect of nanoscale cellular structure on the mechanical properties of Inconel 718 with unique hierarchical structure fabricated by laser powder bed fusion, Acta Mater. 303 (2026), https://doi.org/10.1016/j.actamat.2025.121696.

[5] S. Dixit, S. Liu, H.A. Murdoch, P.M. Smith, Investigating build orientation-induced mechanical anisotropy in additive manufacturing 316L stainless steel, Mater. Sci. Eng. A 880 (2023), https://doi.org/10.1016/j.msea.2023.145308.

[6] J. Barode, M. Brander, T. Yu, V.K. Nadimpalli, D.J. Jensen, X. Wang, Cell structure in LPBF 316L—microstructural heterogeneity, thermal stability, and mechanical properties, Materials 18 (2025), https://doi.org/10.3390/ma18030475.

[7] W. Chen, T. Voisin, Y. Zhang, J.B. Florien, C.M. Spadaccini, D.L. McDowell, T. Zhu, Y.M. Wang, Microscale residual stresses in additively manufactured stainless steel, Nat. Commun. 10 (2019), https://doi.org/10.1038/s41467-019-12265-8.

[8] F.C. Pinto, L.S. Aota, I.R. Souza Filho, D. Raabe, H.R.Z. Sandim, Recrystallization in non-conventional microstructures of 316L stainless steel produced via laser powder-bed fusion: effect of particle coarsening kinetics, J. Mater. Sci. 57 (2022) 9576–9598, https://doi.org/10.1007/s10853-021-06859-1.

[9] I. Morozova, C. Kehm, A. Obrosov, Y. Yang, K.U.M. Miah, E. Uludintceva, S. Fritzsche, S. Weiß, V. Michailov, On the Heat Treatment of Selective-Laser-Melted 316L, J. Mater. Eng. Perform. 32 (2023) 4295–4305, https://doi.org/10.1007/s11665-022-07404-0.

[10] W. Li, L. Meng, X. Niu, W. Zhou, Microstructure, mechanical properties, and deformation behaviour of LPBF 316L via post-heat treatment, Virtual Phys. Prototyp. 19 (2024), https://doi.org/10.1080/17452759.2024.2405623.

[11] A. Yadollahi, N. Shamsaei, S.M. Thompson, D.W. Seely, Effects of process time interval and heat treatment on the mechanical and microstructural properties of direct laser deposited 316L stainless steel, Mater. Sci. Eng. A 644 (2015) 171–183, https://doi.org/10.1016/j.msea.2015.07.056.

[12] E. de Sonis, S. Dépinoy, P.F. Giroux, H. Maskrot, L. Lemarquis, O. Hercher, F. Villaret, A.F. Gourgues-Lorenzon, Dependency of recrystallization kinetics on the solidification microstructure of 316L stainless steel processed by laser powder bed fusion (LPBF), Mater Charact 194 (2022), https://doi.org/10.1016/j.matchar.2022.112370.

[13] P. Dolzhenko, M. Odnobokova, M. Tikhonova, R. Kaibyshev, S.G. Chowdhury, A. Belyakov, Grain boundary assembly in a 316 L steel produced by selective laser melting and annealing, Mater Charact 206 (2023), https://doi.org/10.1016/j.matchar.2023.113434.

[14] X. Chen, X. Xie, J. Hu, X. Li, N. Luo, J. Huang, G. Liang, Experimental and numerical study on the mechanism of interlayer explosive welding, J. Mater. Res. Technol. 30 (2024) 5529–5546, https://doi.org/10.1016/j.jmrt.2024.04.209.

[15] W. Wen, H. Qi, Z. Liao, L. Jiang, M. Huang, B. Yang, Z. Wu, S. Zhou, In-situ study of crack propagation mechanisms in wire arc additive manufactured Al-Mg alloys: Multiple strategies involving microdefects and microstructures, Mater. Sci. Eng. A 924 (2025), https://doi.org/10.1016/j.msea.2025.147802.

[16] W. Ludwig, P. Reischig, A. King, M. Herbig, E.M. Lauridsen, G. Johnson, T. J. Marrow, J.Y. Buffire, Three-dimensional grain mapping by x-ray diffraction contrast tomography and the use of Friedel pairs in diffraction data analysis, Rev. Sci. Instrum. 80 (2009), https://doi.org/10.1063/1.3100200.

[17] V. Muralikrishnan, H. Liu, L. Yang, B. Conry, C.J. Marvel, M.P. Harmer, G. S. Rohrer, M.R. Tonks, R.M. Suter, C.E. Krill, A.R. Krause, Observations of unexpected grain boundary migration in SrTiO3, Scr. Mater. 222 (2023), https://doi.org/10.1016/j.scriptamat.2022.115055.

[18] S. Hata, H. Furukawa, T. Gondo, D. Hirakami, N. Horii, K.I. Ikeda, K. Kawamoto, K. Kimura, S. Matsumura, M. Mitsuhara, H. Miyazaki, S. Miyazaki, M. M. Murayama, H. Nakashima, H. Saito, M. Sakamoto, S. Yamasaki, Electron tomography imaging methods with diffraction contrast for materials research, Microscopy 69 (2020) 141–155, https://doi.org/10.1093/jmicro/dfaa002.

[19] K. Kim, Z. Lee, W. Regan, C. Kisielowski, M.F. Crommie, A. Zettl, Grain boundary mapping in polycrystalline graphene, ACS Nano 5 (2011) 2142–2146, https://doi.org/10.1021/nn1033423.

[20] H.H. Liu, S. Schmidt, H.F. Poulsen, A. Godfrey, Z.Q. Liu, J.A. Sharon, X. Huang, Three-dimensional orientation mapping in the transmission electron microscope, Science 332 (2011) (1979) 833–834, https://doi.org/10.1126/science.1201362.

[21] Y. Zhu, C. Ophus, M.B. Toloczko, D.J. Edwards, Towards bend-contour-free dislocation imaging via diffraction contrast STEM, Ultramicroscopy 193 (2018) 12–23, https://doi.org/10.1016/j.ultramic.2018.06.001.

[22] P.J. Phillips, M.C. Brandes, M.J. Mills, M. de Graef, Diffraction contrast STEM of dislocations: Imaging and simulations, Ultramicroscopy 111 (2011) 1483–1487, https://doi.org/10.1016/j.ultramic.2011.07.001.

[23] C. Ophus, Four-dimensional scanning transmission electron microscopy (4D-STEM): from scanning nanodiffraction to ptychography and beyond, Microsc. Microanal. 25 (2019) 563–582, https://doi.org/10.1017/S1431927619000497.

[24] B.H. Savitzky, S.E. Zeltmann, L.A. Hughes, H.G. Brown, S. Zhao, P.M. Pelz, T. C. Pekin, E.S. Barnard, J. Donohue, L. Rangel Dacosta, E. Kennedy, Y. Xie, M. T. Janish, M.M. Schneider, P. Herring, C. Gopal, A. Anapolsky, R. Dhall, K. C. Bustillo, P. Ercius, M.C. Scott, J. Ciston, A.M. Minor, C. Ophus, Py4DSTEM: a software package for four-dimensional scanning transmission electron microscopy data analysis, Microsc. Microanal. 27 (2021) 712–743, https://doi.org/10.1017/S1431927621000477.

[25] A.D. Darbal, M. Gemmi, J. Portillo, E. Rauch, S. Nicolopoulos, Nanoscale automated phase and orientation mapping in the TEM, Micros. Today 20 (2012) 38–42, https://doi.org/10.1017/s1551929512000818.

[26] L.M. Corrêa, E. Ortega, A. Ponce, M.A. Cotta, D. Ugarte, High precision orientation mapping from 4D-STEM precession electron diffraction data through quantitative analysis of diffracted intensities, Ultramicroscopy 259 (2024), https://doi.org/10.1016/j.ultramic.2024.113927.

[27] P.A. Midgley, A.S. Eggeman, Precession electron diffraction - a topical review, IUCrJ 2 (2015) 126–136, https://doi.org/10.1107/S2052252514022283.

[28] A.C. Diebold, C. Ophus, A. Kordijazi, S. Consiglio, S. Lombardo, D. Triyoso, K. Tapily, A. Mian, N.B.V.I. Shankar, T. Morávek, N. Chandran, R. Stroud, G. Leusink, Template matching approach for automated determination of crystal phase and orientation of grains in 4D-STEM precession electron diffraction data for hafnium zirconium oxide ferroelectric thin films, Microsc. Microanal. 31 (2025), https://doi.org/10.1093/mam/ozaf019.

[29] T. Ronneberg, C.M. Davies, P.A. Hooper, Revealing relationships between porosity, microstructure and mechanical properties of laser powder bed fusion 316L stainless steel through heat treatment, Mater. Des. 189 (2020), https://doi.org/10.1016/j.matdes.2020.108481.

[30] S. Muto, T. Yoshida, K. Tatsumi, Diagnostic nano-analysis of materials properties by multivariate curve resolution applied to spectrum images by S/TEM-EELS, Mater. Trans. (2009) 964–969, https://doi.org/10.2320/matertrans.MC200805.

[31] C.R. Harris, K.J. Millman, S.J. van der Walt, R. Gommers, P. Virtanen, D. Cournapeau, E. Wieser, J. Taylor, S. Berg, N.J. Smith, R. Kern, M. Picus,

S. Hoyer, M.H. van Kerkwijk, M. Brett, A. Haldane, J.F. del Río, M. Wiebe, P. Peterson, P. Gérard-Marchant, K. Sheppard, T. Reddy, W. Weckesser, H. Abbasi, C. Gohlke, T.E. Oliphant, Array programming with NumPy, Nature 585 (2020) 357–362, https://doi.org/10.1038/s41586-020-2649-2.

[32] A.Y. Ng, M.I. Jordan, On Spectral Clustering: Analysis and an algorithm, Adv Neural Inf Process Syst 14 (2001).

[33] E. Schulz, M. Speekenbrink, A. Krause, A tutorial on Gaussian process regression: Modelling, exploring, and exploiting functions, J. Math. Psychol. 85 (2018) 1–16, https://doi.org/10.1016/j.jmp.2018.03.001.

[34] C.E. Rasmussen, C.K.I. Williams, Gaussian processes for machine learning, The MIT Press (2005), https://doi.org/10.7551/mitpress/3206.001.0001.

[35] F. Pedregosa, G. Varoquaux, A. Gramfort, V. Michel, B. Thirion, O. Grisel, M. Blondel, P. Prettenhofer, R. Weiss, V. Dubourg, J. Vanderplas, A. Passos, D. Cournapeau, M. Brucher, M. Perrot, E. Duchesnay, Scikit-learn: machine learning in Python, J. Mach. Learn. Res. 12 (2011) 2825–2830. https://jmlr.org/papers/v12/pedregosa11a.html.

[36] I. MacLaren, A.T. Fraser, M.R. Lipsett, C. Ophus, Digital dark field—higher contrast and greater specificity dark field imaging using a 4DSTEM approach, Microsc. Microanal. 31 (2025), https://doi.org/10.1093/mam/ozae104.

[37] P. Faivre, R.D. Doherty, Nucleation of recrystallization in compressed aluminium: studies by electron microscopy and Kikuchi diffraction, J. Mater. Sci. 14 (1979) 897–919, https://doi.org/10.1007/BF00550722.

[38] P. Trusov, N. Kondratev, M. Baldin, D. Bezverkhy, A Multilevel physically based model of recrystallization: analysis of the influence of subgrain coalescence at grain boundaries on the formation of recrystallization nuclei in metals, Materials 16 (2023), https://doi.org/10.3390/ma16072810.

[39] H. Mao, Q. Liang, Z. Zhang, Y. Du, X. Shuai, G. Zhang, S. Tang, Strain-induced grain boundary migration and grain rotation in polycrystalline metals: atomic-and meso-scale phase field simulations, Comput. Mater. Sci 230 (2023), https://doi.org/10.1016/j.commatsci.2023.112531.

[40] X. Yang, P. Wang, M. Huang, Grain boundary evolution during low-strain grain boundary engineering achieved by strain-induced boundary migration in pure copper, Mater. Sci. Eng. A 833 (2022), https://doi.org/10.1016/j.msea.2021.142532.

[41] P. Snopiński, Effects of KoBo-processing and subsequent annealing treatment on grain boundary network and texture development in laser powder bed fusion (LPBF) AlSi10Mg alloy, Symmetry (Basel) 16 (2024), https://doi.org/10.3390/sym16010122.

[42] Q. He, S. Xia, Q. Bai, Y. Zhang, L. Li, The recrystallization nucleation mechanism for a low-level strained 316L stainless steel and its implication to twin-induced grain boundary engineering, Metall. Mater. Trans. A Phys. Metall. Mater. Sci. 55 (2024) 4525–4542, https://doi.org/10.1007/s11661-024-07548-9.